J. Fluid Mech. (2003), *vol.* 493, *pp.* 59–88.
DOI: 10.1017/S0022112003005998 Printed in the United Kingdom

Observations of inertial waves in a rectangular basin with one sloping boundary

By ASTRID M. M. MANDERS AND LEO R. M. MAAS

Royal Netherlands Institute for Sea Research, P.O. Box 59, 1790 AB Texel, The Netherlands

(Received 9 July 2002 and in revised form 27 February 2003)

Inertial waves in a homogeneous rotating fluid travel along rays that are inclined with respect to the rotation axis. The angle of inclination depends solely on the ratio of the wave frequency and twice the angular frequency. Because of this fixed angle, the waves can become focused when reflected at a sloping wall. In an infinitely long channel with a sloping wall, the repeated action of focusing may lead to the approach to a limit cycle, the so-called wave attractor, where the energy is concentrated. This effect is studied in the laboratory in a rectangular tank with one sloping wall, placed excentrically on a rotating table. The waves are excited by modulation of the background rotation. Several frequency ratios are used to study different wave attractors and one standing wave. The observations consist mainly of particle image velocimetry data in horizontal and vertical cross-sections in one half of the basin. The attractors are observed in the vertical cross-sections. They show continuous phase propagation, which distinguishes them from the standing wave where the phase changes at the same time over the whole cross-section. However, particle motion of inertial waves is three-dimensional and the actual basin is not an ideal two-dimensional channel but is of finite length. This implies that the waves must adapt to the vertical endwalls, although a prediction of the nature of these adaptations and the structure of the three-dimensional wave field is at present lacking. For critical waves, whose rays are parallel to the slope, clear three-dimensional behaviour is observed. The location of most intense motion along this critical slope attractor changes in the horizontal direction and horizontal phase propagation is observed, with a wavelength between 1/5 and 1/4 of the basin length. For the other attractors there is little evidence of phase propagation in the horizontal direction. The motion along the attractor is however stronger near the vertical endwalls for attractors with wave rays of slopes close to 1 or larger. The standing wave and the other attractors are more clearly visible near 1/5 of the tank length.

1. Introduction

Fluids in solid-body rotation are stably stratified in angular momentum (e.g. Greenspan 1968*b*). In the same way that a fluid, stably stratified in density, can support internal gravity waves, a fluid in solid-body rotation can carry inertial waves. These are sometimes called gyroscopic waves to distinguish them from the limiting case of inertial oscillations in a rotating, density-stratified fluid, when the frequency equals twice the rotation frequency (LeBlond & Mysak 1978). Inertial waves and internal waves share the property that their vertical direction of propagation is restricted. It depends on the wave frequency and, respectively, on the rotation rate and the strength of the stratification. They travel obliquely through the fluid, as

shown experimentally by Görtler (1943) for internal waves and Oser (1958) for inertial waves. Owing to the strong analogy between inertial and internal waves for two-dimensional flow (Veronis 1970), it is possible to investigate internal waves and thereby obtain information on inertial waves. This justifies the inclusion of results on internal waves in the discussion. The most important difference between these waves is that internal wave particle motion is rectilinear, so that in a three-dimensional container two-dimensional waves can also be realized, whereas inertial wave particle motion is intrinsically three-dimensional (circular) due to the Coriolis force, which gives inertial waves a distinct three-dimensional character.

The restriction on the propagation direction has consequences for reflection. In general, the waves do not reflect according to Snell's law, but will be focused or defocused (Phillips 1963), since parallel incident wave rays must remain parallel after reflection. The only exceptions are walls that are parallel or perpendicular to the rotation axis or the direction of gravity, for inertial and internal waves respectively. In an enclosed basin, if focusing is not balanced by defocusing, repeated reflection will lead to the appearance of a limit cycle. This cycle is called the *wave attractor* (Maas & Lam 1995) since all wave rays will approach this cycle. Here the wave energy is concentrated. But the wave rays will not actually reach this cycle in finite time (Greenspan 1968*a*).

The notion of such 'pathological' behaviour in fluids is quite old. Görtler (1943, 1944) mentioned that there might be regularity problems along the wave rays, which may disappear if viscosity is taken into account. Stern (1963), Bretherton (1964), Stewartson & Rickard (1969) and Stewartson (1971, 1972) found trapping of low-frequency oscillations near the equator for a thin spherical shell, all using different concepts and approximations. Israeli (1972) found that this trapping does not occur for isolated frequencies but for continuous frequency intervals, bounded by frequencies for which reflection takes place at critical latitudes of the inner and outer sphere. Numerical models were used to further study the occurrence and behaviour of the wave attractors, and the structure of the shear layers that occur when viscosity is included in the model (Rieutord, Georgeot & Valdettaro 2001).

The spherical shell is a geometry of special interest in geophysics (oceans, liquid outer core of the Earth) and astrophysics (stars). But there are other geometries for which wave focusing towards a limit cycle takes place. A relevant case is an internal wave approaching a beach, represented by a wedge. If the bottom slope is less steep than the slope of the wave ray, the wave energy can be reflected up-slope. After repeated reflection at the surface and the bottom the wave approaches the corner of the wedge (Wunsch 1969), which can then be interpreted as a (point) attractor. Maas & Lam (1995) investigated internal waves reflecting in different simple geometries and found various attractors for a parabolic basin and a trapezoidal basin ('bucket'). They also investigated the distribution of attractors in frequency space and found a self-similar structure with small frequency intervals with weak attractors between the larger frequency intervals with stronger attractors.

The studies mentioned so far are purely theoretical work. In laboratory experiments one often works with basins in which no wave focusing takes place, with basin walls parallel or perpendicular to the axis of rotation or the direction of gravity. This reveals a discrete set of standing waves. The rotating cylinder is particularly widely studied. McEwan (1970) studied standing waves, corresponding quite well to inviscid linear predictions, but he also reported a resonant collapse for larger amplitudes, leading to disorder. Manasseh (1992) reports various breakdown mechanisms for standing waves in a rotating and precessing cylinder. Aldridge & Toomre (1969) observed standing

inertial waves in a rotating sphere, a geometry for which focusing is balanced by defocusing.

Experiments in which internal gravity wave energy is attracted towards the corner of a wedge were carried out by Wunsch (1969) and Cacchione & Wunsch (1974). Greenspan (1968*a*) and Beardsley (1970) investigated this for inertial waves in a cone. Beardsley (1970) also observed inertial waves in a truncated cone. Such a geometry has the same cross-section as the bucket described by Maas & Lam (1995) and enables focusing. Although Beardsley interpreted his results in terms of standing waves, they can be interpreted alternatively in terms of wave attractors, as will be argued in the discussion, in § 5.

A visually clear experimental realization of an internal wave attractor that is really a limit *cycle* was done by Maas *et al.* (1997) in a rectangular tank with a sloping sidewall for internal gravity waves. This is the most simple geometry in which to study wave focusing towards an attractor. That this is also the case for inertial waves in a homogeneous, rotating fluid was shown by Maas (2001).

In the present study, the experiments described in Maas (2001), where a single inertial wave attractor is observed, are extended. We use different forcing frequencies to generate attractors of different shape and one standing wave. The predicted boundaries of the frequency interval over which the most simple attractor exists are checked experimentally, and the difference with the standing wave will be illustrated. We took measurements at various horizontal and vertical cross-sections to investigate the changes of the wave field in the horizontal direction.

The results by Maas (2001) already confirm that focusing towards an attractor, predicted by the two-dimensional theory, exists. However, because of the intrinsic three-dimensional nature of inertial waves, the finite extent of the basin is expected to influence the horizontal structure of the wave field. Since we have not been able to solve the Poincaré equation that describes the full three-dimensional wave field (as is possible for a rectangular tank without a sloping wall, Maas 2003), we depend on the experimental results to obtain insight in the three-dimensional structure. In the next section the theory of inertial waves will be briefly outlined and the concept of a wave attractor illustrated. Then the experimental set-up is discussed. To illustrate the attractor shapes, results of measurements in vertical cross-sections are shown. Next, vertical cross-sections at different positions are compared to study changes in the horizontal direction and a small selection of measurements in horizontal cross-sections will be presented. Finally the results are discussed.

2. Theory

The basic equations governing a rotating inviscid homogeneous fluid are the momentum equations and the continuity equation. In this paper we will consider waves in a frame of reference that is in nearly solid-body rotation. The angular velocity of the frame will be $\Omega = \Omega_0 + \epsilon\Omega_1(t)$, where Ω_0 is the background rotation rate while $\Omega_1(t)$ is its time-periodic modulation. The strength of the periodic modulation ϵ ($\ll 1$) determines the scale of the perturbations. The linearized momentum equations for the perturbation velocities and perturbation pressure then are

$$\frac{\partial u}{\partial t} = 2\Omega_0 v + y\frac{\partial \Omega_1}{\partial t} - \frac{\partial p}{\partial x}, \tag{2.1a}$$

$$\frac{\partial v}{\partial t} = -2\Omega_0 u - x\frac{\partial \Omega_1}{\partial t} - \frac{\partial p}{\partial y}, \tag{2.1b}$$

$$\frac{\partial w}{\partial t} = -\frac{\partial p}{\partial z}, \tag{2.1c}$$

with u, v, w the perturbation velocity components in the x-, y- and z-directions with z parallel to the rotation axis. The gradient of the pressure P and gravitational and centrifugal forces form a dynamic equilibrium at zeroth order. In the linear equation, they are combined in the perturbation pressure term $p = P - (x^2 + y^2)\Omega^2/2 + \rho g z$, where ρ denotes the uniform density and g the acceleration due to gravity.

The remaining right-hand-side terms due to rotation and modulation of the frame are the Coriolis and Euler force respectively (Tolstoy 1973). The continuity equation is

$$\nabla \cdot \boldsymbol{u} = 0. \tag{2.2}$$

At solid boundaries the normal velocity of the fluid must vanish, leading to the boundary condition

$$\boldsymbol{u} \cdot \boldsymbol{n} = 0, \tag{2.3}$$

with $\boldsymbol{n}$ the outward normal.

In the experiments, we are interested in the inertial wave field. The behaviour of these waves for a uniformly rotating fluid ($\Omega_1 = 0$) will be treated first, then the generation of these waves via modulation of the angular frequency ($\Omega_1 \neq 0$) will be discussed.

2.1. *Inertial waves*

In this subsection we look at a free monochromatic wave $\propto \exp(-\mathrm{i}\omega t)$ of frequency ω in a uniformly rotating fluid with angular velocity Ω_0. Equations (2.1 *a–c*) and (2.2) can then be reduced to a single equation for the pressure:

$$p_{xx} + p_{yy} - \lambda^2 p_{zz} = 0 \tag{2.4}$$

with

$$\lambda^2 = \frac{4\Omega_0^2 - \omega^2}{\omega^2}. \tag{2.5}$$

This so-called Poincaré equation (Cartan 1922) can be reduced to two dimensions by assuming an infinitely long channel in the y-direction and y-independent waves, so that derivatives with respect to y vanish. The resulting two-dimensional equation is a wave equation (hyperbolic equation) if $\omega < 2\Omega_0$. Note that, due to the Coriolis force, the *particle* motion itself does have a component in the y-direction, as can be seen from the linearized Euler equations (2.1 *a–c*).

For a very limited class of two-dimensional geometries, the wave equation can be solved using separation of variables. The boundaries must then be parallel or perpendicular to the rotation axis (rectangular), with the circle (or more generally, the ellipse) as an exception. The solution then reveals a discrete set of standing waves. For an arbitrary geometry one can use the method of characteristics. These characteristics correspond physically to rays along which the energy propagates (see Maas & Lam 1995). Every characteristic carries information on the pressure on the boundary into the interior. Along a characteristic, the *partial pressure* (half the pressure on the boundary) is conserved. At a point in the interior, the pressure is the sum of the partial pressure values on each of the two characteristics through this point.

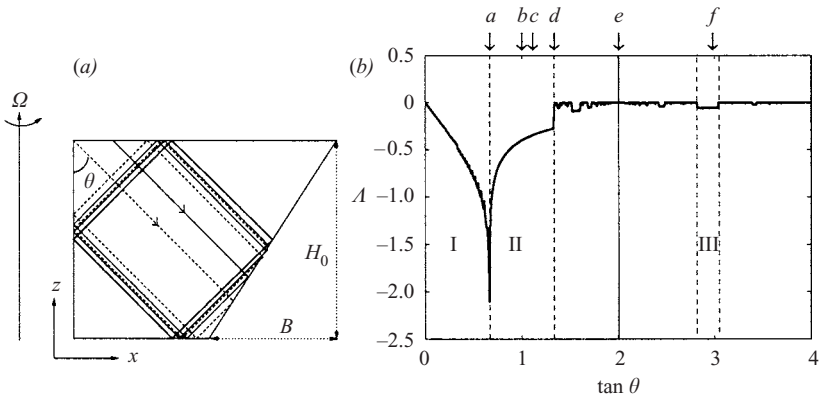

FIGURE 1. (*a*) Cross-section of a rectangular basin with sloping sidewall. Two parallel wave rays (thin solid and dashed lines), making an angle θ with the rotation axis, reflect and their distance apart decreases (focusing). They approach a limit cycle (thick solid square) due to repeated focusing at the sloping wall. (*b*) Lyapunov exponent Λ as a function of the slope of the characteristics with respect to the rotation axis. It illustrates that wave attractors occur over an interval (window) in parameter space. Interval I: all wave rays are attracted towards the upper right corner. Interval II: (1,1)-attractor. Interval III: (1,3)-attractor. Solid line: (1,2) standing wave. In general: the more complex the structure, the weaker the attractor and the smaller the window in which it occurs. The arrows indicate the values of $\tan\theta$ for which experiments are carried out. The corresponding labels refer to the (attractor) shapes shown in figure 2.

If one substitutes the plane wave solution $p(x, z) = \mathscr{P} \exp \mathrm{i}(kx + mz)$, the dispersion relation is

$$\frac{k}{m} = \pm\lambda. \tag{2.6}$$

This shows that for a given frequency only four directions of propagation are possible. Phillips (1963) gives a very general treatment of the physics of these waves. Wave energy travels along characteristics (wave rays) $x \pm z\tan\theta = \text{const}$, with $\tan\theta = 1/\lambda$ the slope of the group velocity vector with respect to the rotation axis. Lines of equal phase are parallel to these rays. The phase propagates in a direction perpendicuar to the energy, with the horizontal component opposite to the horizontal direction of energy propagation.

2.1.1. *Wave attractors*

For reflection at boundaries parallel and perpendicular to the rotation axis, incoming and reflected waves are symmetric with respect to the normal of the boundary, and nothing special occurs. However, for an arbitrarily sloping wall, the symmetry with respect to the normal is broken because of the constraint on the direction of propagation. Hence waves will be geometrically focused or defocused. In an enclosed basin repetitive focusing can lead to the appearance of a 'wave attractor', a limit cycle where ultimately all wave energy ends, although not in finite time (Greenspan 1968*a*). In figure 1(*a*) this is illustrated for the most simple case: a rectangular basin with one sloping sidewall. This sloping sidewall provides the possibility of wave focusing. Every time a wave ray reflects downwards from this wall it gets closer to the limit cycle, the central square. This limit cycle is the only periodic orbit for this frequency. The period is defined as the number of reflections for this orbit to close onto itself. The total convergence or divergence along a wave

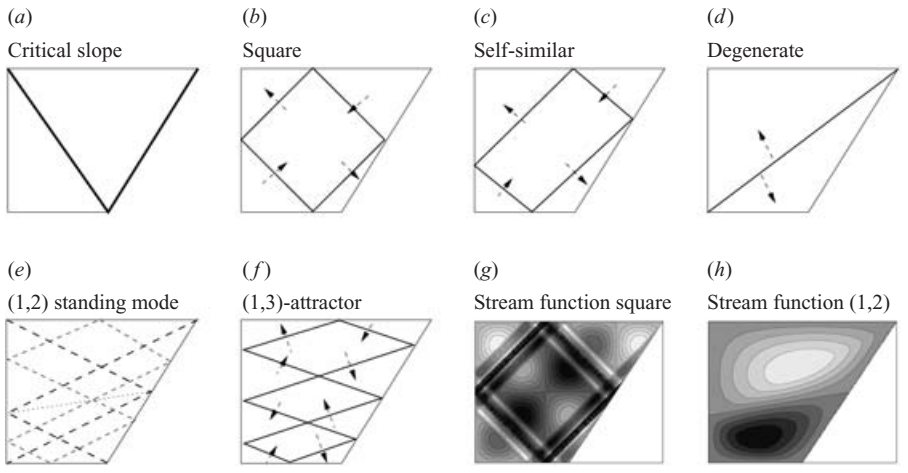

FIGURE 2. Shapes of the attractors and the resonant mode in terms of wave ray paths (solid lines) with direction of phase propagation indicated with arrows in (*b–d, f*); corresponding stream function of square attractor (*g*) and (1,2)-mode (*h*). See text for more explanation.

ray is represented by the Lyapunov exponent Λ (Maas & Lam 1995). Negative values indicate convergence; positive values do not occur for this system, since the parameter space is one-dimensional (Rieutord *et al.* 2001). The value of Λ is proportional to $\log|(\lambda - s)/(\lambda + s)|$ where $s = H_0/B$ is the slope of the wall. Its only singularities occur for $\lambda = \pm s$ when critical reflection causes immediate focusing and $\Lambda \to -\infty$. Λ is inversely proportional to the period of the attractor (Maas & Lam 1995). A wave attractor exists over a parameter interval. Over this interval, the attractor gradually deforms, but the number of reflections at the boundary of the limit cycle is constant. The intervals are bounded by values for which the attractor degenerates, connecting two corners of the basin. Standing waves exist for isolated frequency values, when focusing is exactly balanced by defocusing. Then all wave rays return back onto themselves and $\Lambda = 0$. They are surrounded by frequencies for which the attractor period approaches infinity and hence the Lyapunov exponent approaches zero.

We wish to study a number of patterns experimentally. The simplest attractor is called a (1,1)-attractor, since it has one reflection at the bottom and one reflection at the sloping wall. It is investigated for several values in the frequency interval of its existence (window, interval II figure 1*b*), including the limiting values. The corresponding shapes are illustrated in figure 2(*a–f*). On approaching the lowest value of $\tan\theta$, the (1,1)-attractor appears as a diagonal line from the upper left corner to the lower right corner. For the specific geometry with the bottom length being half the top length, this coincides with the frequency at which the wave rays are parallel to the slope, which results in a single V-shaped structure (figure 2*a*). This combination of attractors is called the 'critical slope' attractor and $\Lambda \to -\infty$ due to the immediate focusing at the wall. This immediate focusing at the sloping wall removes the possibility of focusing towards the diagonal structure, but when the wave energy propagates parallel to the slope and reflects at the bottom it will travel along this diagonal. For increasing θ, the pattern changes towards a parallelogram, with the square (figure 2*b*) and self-similar (figure 2*c*) attractor as examples. The latter is called self-similar since reflection at the top and the bottom of the tank occurs at positions where the relative distances to the left and right corners are identical. The

upper limit is reached when the attractor degenerates into a single line connecting the upper right to the lower left corner (figure 2*d*).

The next simple closed structure has one reflection at the bottom and two reflections at the sloping wall (figure 2*e*). However, this (1,2)-structure is not an attractor. Focusing for the downward reflection at this wall is cancelled exactly by the other, upward, reflection. So every ray reflects back onto itself. The result is a standing wave mode for which the stream function consists of two (counter-rotating) cells (figure 2*h*), separated by the line on which every ray intersects itself (dotted in figure 2*e*). This is in remarkable contrast to the square attractor, of which the stream function has patterns that are repeated but become extremely small close to the attractor (figure 2*g*). In figure 2(*e*), the characteristics connecting the corners of the basin are plotted (thick dashed lines); where they intersect there is no motion: these two points are the centres of the two cells. The other dashed line shows an arbitrary characteristic, returning back onto itself. This mode exists for a single isolated frequency.

The most complicated structure that is studied is the (1,3)-attractor, which exists over a much smaller frequency interval than the (1,1)-attractor (interval III in figure 1*b*, shape illustrated in figure 2*f*). Convergence is weaker than for the (1,1)-attractors (Λ less negative), due both to the fact that focusing is weaker for this value of θ and to the larger period.

In frequency space, between these attractors all kinds of complicated weak attractors and standing modes exist, as illustrated by Maas *et al.* (1997) and as can be seen from figure 1(*b*). They will be more difficult to realize and observe experimentally.

2.1.2. *Three-dimensional aspects*

So far the inertial wave problem has been reduced to a two-dimensional problem. It is extremely difficult to solve the inertial wave field in three dimensions. No general solution is available, and one needs a simplifying argument like separation of variables (Stewartson & Rickard 1969), which is only possible for a limited class of domain shapes (a cylinder (Kelvin 1880), a sphere (Bryan 1889) and a rectangular box (Maas 2003)), and even then only when the main axes of the domains are parallel and perpendicular to the rotation axis.

Unlike for internal gravity waves, where particle motion is truly two-dimensional (rectilinear), there is particle motion in the y-direction due to the Coriolis force. Particles move anticyclonically along circles in planes along the characteristics $x \pm z\tan\theta = \text{const}$. Only the projection of this motion on the (x, z)-plane yields rectilinear motion for plane waves. In a finite basin, the two-dimensional structures must be modified by the frontwall ($y = 0$) and endwall ($y = L$) in order to fulfil the boundary condition of no flow. This could result in a standing wave structure in the y-direction, if the wavelength in the y-direction matches the dimensions of the basin. It is also possible that waves travel along the attractor in the horizontal direction, thus describing a kind of helix through the basin.

A phenomenon that could be encountered is a combination of inertial Poincaré and Kelvin waves (Maas 2003). These waves are the purely inertial counterparts of the conventional Poincaré and Kelvin waves, which are rotationally modified gravity waves (LeBlond & Mysak 1978). Assuming standing waves in the vertical, in a rectangular tank inertial Poincaré and Kelvin waves combine to give patterns in the horizontal direction for eigenfrequencies of the system. Typically, modal structures were obtained, with regions moving in unison, and amphidromes, with phase lines circling around them. In the horizontal, particle motion is dominantly anticyclonic. The resulting patterns have small-scale structures near the walls of the basin and

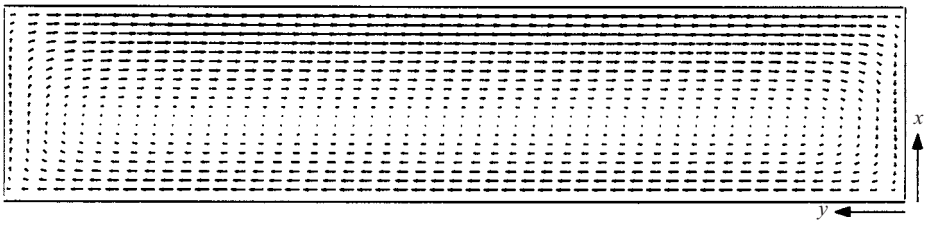

FIGURE 3. Calculated vorticity-conserving horizontal flow for the tank with sloping wall. The sloping part occupies the upper half of the figure. The centre of the flow cell is above the flat part of the bottom.

increase in scale with increasing frequency. Whether these waves lead to similar structures in a basin with a sloping wall is still an open question.

2.2. *Vorticity-conserving flow*

In the previous section free waves were considered. In the experiments, these are generated via continuous weak modulation of the rotation rate $\Omega_1(t) = \Omega_0 \sin \omega t$. The fluid, previously considered as being in solid-body rotation, will react on changes in Ω by the generation of a vorticity-conserving horizontal flow.

There are two mechanisms via which inertial waves are excited. First, the horizontal vorticity-conserving flow has a component through the sloping wall, which will be compensated by the generation of waves. In a cylindrical container, this inviscid mechanism is not operating, since the vorticity-conserving flow would be everywhere parallel to the walls. In that case only the second generation mechanism applies: Ekman pumping and suction. The flow parallel to the boundaries generates Ekman layers in which fluid transport converges and diverges periodically, which generates waves (Aldridge & Toomre 1969).

The forced equations with time variations of the angular frequency form a system that is closely related to the spin-up problem of a container with a sloping bottom that was studied by van Heijst, Maas & Williams (1994). For a shallow tank ((height/length)$^2 \ll 1$) the shallow-water approximation was used to enable the calculation of an analytical solution. This implies vertically uniform solutions, which is only an approximation of the actual flow field. However, the exact solution for the problem of a wedge-shaped container shows that the flow is nearly vertically uniform for the ratio of height H_0 and length L in the tank that will be used in our experiments. This justifies the use of the shallow-water approximation.

Therefore, we solved the shallow-water equations for the basin with one sloping wall. This can be done without further approximations. The detailed derivation of the flow field can be found in the Appendix. The resulting horizontal velocity field is plotted in figure 3. The pattern of the vorticity-conserving flow will change sinusoidally with time. To obtain absolute velocities, the expressions found in the Appendix must be multiplied by a factor $A\bar{r} \sin \omega t$. Here $\bar{r}$ is the distance from the centre of the tank to the rotation axis and A an amplitude factor chosen to match the observed vorticity-conserving flow, which appeared to be close to 1 (to within 20% for the various observations). The inviscid forcing mechanism appears particularly relevant near $y = 0$ and $y = L$ where the flow is predominantly cross-isobath.

We have not been able to explicitly link the vorticity-conserving flow and the inertial wave field. However, the inertial wave field in the vertical is expected to be dominated by wave attractors, whose location is independent of the forcing location and mechanism.

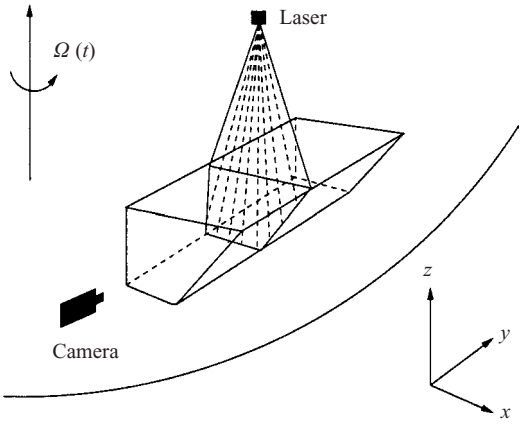

FIGURE 4. Schematic of experimental set-up.

	Name	Period (s)	$\omega/2\Omega_0$	$\tan\theta$
(*a*)	critical slope	43.17	0.5558	0.6685
(*b*)	square	33.89	0.7092	1.0000
(*c*)	self-similar	32.24	0.7445	1.1150
(*d*)	degenerate	29.97	0.8006	1.3362
(*e*)	(1,2) standing	26.82	0.8950	2.0060
(*f*)	(1,3)	25.32	0.9481	2.9802

TABLE 1. Applied modulation periods and corresponding parameter values.

3. Experimental set-up

The experiments were carried out on the 13 m diameter rotating platform of the Coriolis Laboratory (Grenoble, France). The set-up is a larger version of the one described in Maas (2001). A schematic of the set-up is shown in figure 4. On the platform, a tank with size $107 \times 500 \times 80$ cm^3 (width $2B \times$ length $L \times$ height H_0) was placed near the outer rim ($\bar{r} \approx 4$ m). A sloping wall was placed in the tank, reaching from the outer upper corner to halfway to the bottom ($x = B = 53.5$ cm). The tank had a glass front and a lid consisting of glass plates of 107×100 cm^2 with metal strips around them. The tank was filled with ordinary tap water.

The platform was rotated with a background period of 48 s ($\Omega_0 = 0.13$ rad s^{-1}). To generate the waves of frequency ω, as indicated, the rotation speed was perturbed periodically with a small-amplitude perturbation, $\Omega = \Omega_0(1 + \epsilon \sin \omega t)$. The amplitude of 8 cm s^{-1} of the modulation at the outer rim of the platform, relative to the background rotation velocity of 85 cm s^{-1}, yields $\epsilon \approx 0.1$. The velocities of the vorticity-conserving flow have maximum values of about 1.5 cm s^{-1} relative to the rotating platform. In table 1 the modulation periods employed, the frequency ratio $\omega/2\Omega_0$ and $\tan\theta$ are given.

For visualization of the flow almost neutrally buoyant particles were added to the water. These were illuminated by a sheet of laser light approximately 2 cm thick. The particles within this sheet were detected by a digital camera (768×484 pixels, frame rate 30 Hz). With particle image velocimetry (PIV) (Fincham & Spedding 1997) the pictures taken by the camera were translated into velocity vector fields after every 90 frames, using a subset of these frames. The ultimate results of these measurements

are series of two-dimensional velocity fields on a 62×46 grid with time intervals of 3 to 4 s, depending on the exact frame subset settings. Particle motion in the direction perpendicular to the laser sheet cannot be detected, so the vector fields represent a projection of the motion onto the plane. Measurements were taken in (x, z)-planes ('vertical cross-sections') like those illustrated in figure 4 and in (x, y)-planes ('horizontal cross-sections') where the position of the laser and the camera were interchanged.

Measurements of vertical cross-sections were taken from $y = 60$ to 210 cm; measurements closer to the front wall ($y = 0$) and further into the basin caused practical difficulties. Measurements of horizontal cross-sections cover only a small part of the tank. This is because the camera cannot cover more than about $80 \times 100\,\mathrm{cm}^2$ in the (x, y)-plane, at the height at which it was placed. The depth range of the measurements is from $z = 23$ to 63 cm. Only the self-similar and square attractor measurements were taken at two different y-positions.

For the vertical cross-sections a time series consists of 120 vector fields, covering about 16 wave periods. For the horizontal cross-sections a time series consists of 200 vector fields, spanning about 25 wave periods. In order to observe the wave field in the horizontal cross-sections, the vorticity-conserving flow must be subtracted from the measurements. Using the theoretically predicted vorticity-conserving flow field with an experimentally determined amplitude factor, this otherwise dominant flow was accounted for. The vertical cross-sections are hardly affected by the vorticity-conserving flow, since for the locations of these cross-sections, this flow is mainly perpendicular to the (x, z)-plane.

To compare cross-sections at different locations and for different forcing frequencies, they should have the same phase with respect to the forcing. This was not arranged automatically in the experiment. Therefore, the time series must be reordered such that every series starts with the same phase. For the horizontal cross-sections this can be done using the phase of the vorticity-conserving flow, which is easy to determine. In the vertical cross-sections the vorticity-conserving flow can hardly be seen and a different method is needed. We can use the idea that a horizontal and a vertical cross-section must show the same values for the u-component at their line of intersection, when these sections represent the same phase of the flow. One can determine for which time shift of the vertical time series the u-components on this line match those of the horizontal cross-sections. The time shift combined with the correctly determined phases for the time series of the horizontal cross-sections results in phases for the time series of the vertical cross-sections. To increase the accuracy of this method (an error in the phase of 10–20° is possible), a single vertical cross-section series was matched with all the horizontal series available for that location. This gives fairly consistent results, except for the (1,3)-attractor and at $y = 60$ cm for the (1,2)-mode.

Further the data can be rearranged such that instead of a long time series with few measurements per period one obtains a single period with high frequency sampling rate ('asynchronous sampling'). This is illustrated in figure 5 for synthetic data. It can only be used if the observed system is stationary and the motion has frequencies that are multiples of the modulation frequency. Then also frequencies that are higher than the original sampling frequency can by resolved and aliasing is prevented.

In addition to the PIV measurements, experiments with dye were performed to observe the large-scale flow. Also an experiment with a different forcing mechanism was done: the tank was not modulated but a paddle over the full length of the tank was oscillated in the upper left corner. Because of practical problems with the paddle, only a few experiments could be performed.

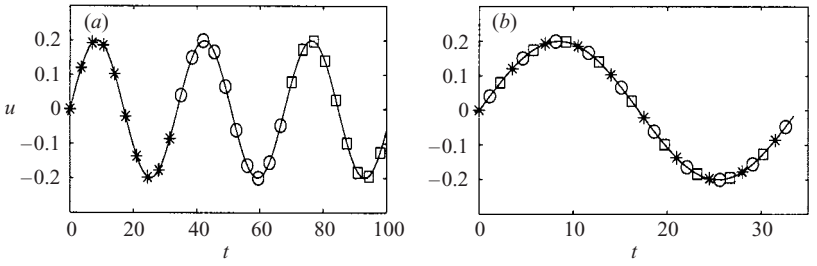

FIGURE 5. Example of asynchronous sampling and reorganization of data. (*a*) Synthetic time series. (*b*) The same data points, but rearranged with respect to the phase of the vorticity-conserving flow and with the application of asynchronous sampling.

4. Results

The first aim of the experiments was to find the theoretically predicted attractors. Therefore, we start with results from the vertical cross-sections. First, results for a fixed y-coordinate are shown to compare with the theoretically predicted patterns. Then the variation of these patterns with the y-coordinate will be discussed, with emphasis on the critical slope and the self-similar attractor. Finally the results for the horizontal cross-sections are presented.

All results will be presented in scaled coordinates. The x-coordinate is scaled with the half-width of the tank $B = 53.5\,\text{cm}$, the y-coordinate with the length $L = 500\,\text{cm}$ and the z-coordinate with the height $H_0 = 80\,\text{cm}$.

4.1. *Vertical cross-sections*

4.1.1. *Visualization of attractors*

The results of PIV are vector fields. In these vector fields one can often observe relatively strong motion around the location of the theoretical attractor. But these vector fields are just snapshots of time-varying motions; they do not fully represent the behaviour of the wave field. Furthermore, particle motion has a component of motion in a plane perpendicular to the plane of observation. So we measure only a projection of the motion.

To get an idea of the motion over a whole period, hodographs (lines joining the tips of the velocity vectors) were made. The asynchronous sampling method was used and seven vector fields with about the same phase were averaged. This can be justified since the motion appears to be periodic; the forcing frequency is by far the most dominant in the spectrum. An example is plotted in figure 6(*a*). It illustrates that over a period, velocity vectors describe ellipses. On the attractor itself (see also figure 2*c*), these can be long and narrow, with the major axis aligned along the attractor. This is consistent with the theoretical prediction of circular motion with the other component of motion in a plane perpendicular to the plane of observation. Where the attractor reflects from the boundaries, the motion is nearly circular: clockwise for reflection at the top and bottom, anticlockwise for reflection at the straight and sloping sidewalls, except at the wall itself where it must be parallel to the wall. This pattern can be explained by considering a beam of wave rays that reflects from a wall. The combination of an incoming and a reflected wave ray yields motions that add up to motions that are not parallel to one of the individual wave rays. Over a period, the projection of the motion can then be an ellipse, with ellipticity and orientation depending on the location in the beam.

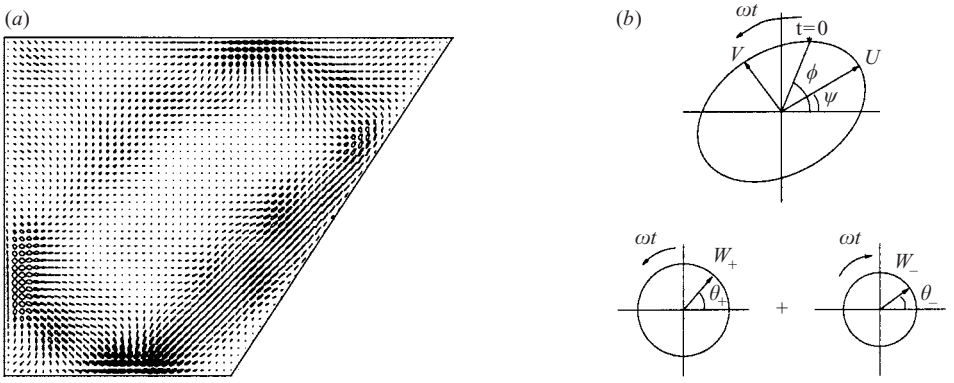

FIGURE 6. (*a*) Hodographs of self-similar attractor (arbitrary scaling; table 1, case *c*), based on asynchronous sampling of 120 measurements and averaging per seven measurements with nearly identical phase. For the solid ellipses motion is clockwise, for the transparent ellipses motion is anticlockwise. (*b*) Decomposition of such an ellipse into two counter-rotating circles.

Therefore, it seems natural to use ellipse parameters to describe the observed patterns. This is illustrated in figure 6(*b*). The ellipse can be characterized by its main axes U and V, phase φ and orientation ψ. However, when motion is nearly circular, slight perturbations determine the orientation ψ and therefore φ, resulting in incoherent pictures with phase jumps. Also, in our definition ψ varies between 0 and 360°, with the consequence that φ is between 0 and 180°, rather than the other (physically desirable) way round. In order to circumvent this, the ellipse is decomposed into two circles, one traversed clockwise and the other anticlockwise. These two circles are characterized by their radius W_- and W_+ and 'phase' θ_- and θ_+, with $U = W_+ + W_-$, $V = W_+ - W_-$, where V will take negative values for clockwise motion, $\varphi = (\theta_- - \theta_+)/2$ and $\psi = (\theta_+ + \theta_-)/2$. A more detailed description of this decomposition can be found in Maas & van Haren (1987). When interpreting pictures of θ_-, one must keep in mind that the smaller θ_-, the larger the true phase, since θ_- is defined as the anticlockwise angle with the horizontal axis, whereas the circle is traversed in a clockwise sense (figure 6*b*). The advantage of this decomposition is that the time series can be summarized in a few pictures, with the restriction that flow other than this ellipsoidal motion with frequency equal to the forcing frequency is filtered out. Nevertheless, since ellipsoidal motion is thought to represent the field we are interested in, and it is clearly the dominant frequency in the spectrum, this approach is justified.

The observations are presented in terms of U, θ_+ and θ_-. The major axis U represents the intensity of motion. The minor axis V shows the deviation from rectilinear motion. They are not shown separately, since they only seem to be significant near the walls, where the waves reflect. The phases θ_+ and θ_- do not represent the physical phase of the wave, since only a projection of the full three-dimensional motion is considered. Still, these phase parameters indicate the propagation of the waves in the (x, z)-plane.

Pictures of U, θ_+ and θ_- of all the different attractors and the standing wave mode are shown in figure 7 for $y = 0.24$. At this y-coordinate a two-dimensional description can be justified, since it is not close to a vertical endwall and the vorticity-conserving flow is directed almost purely along the y-axis. It appears that all the predicted structures are visible here. The colour scale is equal for all attractors. The pictures are

constructed such that they start with the same phase with respect to the sinusoidal forcing ($t = 0$), except for the (1,3)-attractor for which this phase was not determined well. They are again based on asynchronous sampling and averaging over seven vector fields with nearly the same phase.

In some pictures one can observe a narrow band from the top ($x \approx 1$) to the bottom ($x \approx 0.5$). This is caused by the laser. The laser beam is turned into a laser sheet by a prism to illuminate the fluid. But there is still a trace of the direct ray, which perturbs the measurements. In the data processing, we interpolated to get rid of this perturbation, but it is not always equally successful.

The *critical slope attractor* is not very visible; only the part near the sloping wall shows intense motion. There is relatively more motion outside the attractor, compared with the other frequencies. From the pictures of θ_+ and θ_- the V-shape is more clear. Lines of equal phase are roughly aligned along the attractor for θ_- near the sloping wall. The other part of the attractor coincides with the rapid phase changes. Outside the attractor, the phases vary smoothly over the plane and lines of equal phase are not strictly parallel to wave rays.

The *square* and *self-similar attractor* are clearly visible. Motion is most intense near the sloping wall, where the focusing takes place. On following the attractor in clockwise sense, the intensity decays. Outside the attractor there is not much motion. Phase lines are parallel to the attractor. The theoretical directions of phase propagation, based on clockwise energy propagation along the attractor, are reproduced well by the observations: phase propagates outwards for characteristics with positive slope and inwards for characteristics with negative slope. In the middle of the cross-section, far away from the attractor, motion is weak. The observed phases cannot be fully relied on then, but structures are spatially coherent which gives the results credibility.

Phase lines of θ_+ circle around the top and bottom reflection points of the attractor, where the ellipses are completed in a clockwise direction. Phase lines of θ_- circle around the sidewall reflections of the attractor, where the ellipses are completed in an anticlockwise direction. This can be explained by the fact that at the location where all phase lines meet (amphidromic points) this phase is meaningless since the corresponding motion W_+ or W_- vanishes there.

The *degenerate attractor* is rather weak and the line of maximum U is a little below the predicted attractor location. There is a sharp phase contrast at the location of the theoretical attractor. This suggests that particle motion on one side of the degenerate attractor is opposite to that on the other side, which gives rise to high shear around it, such that the attractor itself is not visible.

The *(1,2)-mode* looks like a weak attractor at first sight. Motion is concentrated around a particular characteristic. On the line that connects the upper right corner to the lower right corner velocities are (nearly) zero (see figure 2*e*). Motion is clearly less intense than for the square and self-similar attractor. Phase lines are not everywhere parallel to the wave rays. The sharp phase contrast corresponds to the line connecting the upper right corner to the lower right corner of the basin, through the centres of the counter-rotating cells. Evidence that this is a standing mode and not an attractor will be given below.

The *(1,3)-attractor* is relatively weak. For this frequency, focusing is weaker than for the (1,1)-attractor. Also, the attractor length (perimeter) is larger so that viscous losses along the attractor may become more important. In the vertical, the scale of the attractor is smaller than for the square and self-similar attractor. Where two parts of the attractor with opposed particle motion are close together, they may interact due to viscous effects, also reducing the strength of the motion. The location of high

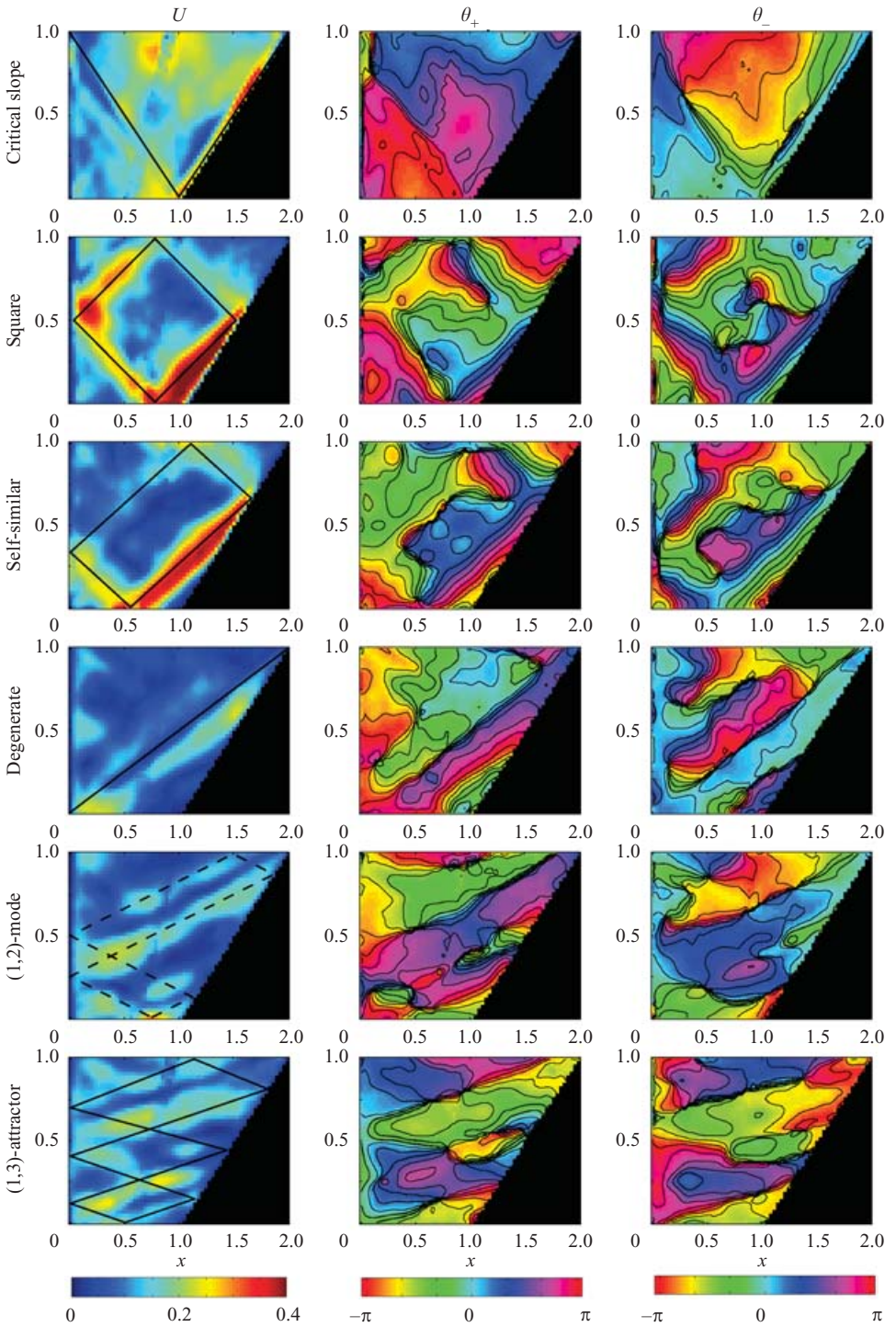

FIGURE 7. Decomposition of hodographs (figure 6) for (1,1)-attractors (critical slope, square, self-similar and degenerate attractors), standing (1,2)-mode and (1,3)-attractor at $y = 0.24$. The scale for U ranges from 0 (dark blue) to $0.4\,\mathrm{cm\,s^{-1}}$ (dark red). The colour scale for $\theta_{+,-}$ is periodic. The black lines indicate the theoretically predicted attractor. For the (1,2)-mode a single, somewhat arbitrary periodic characteristic that matches the pattern is plotted (dashed).

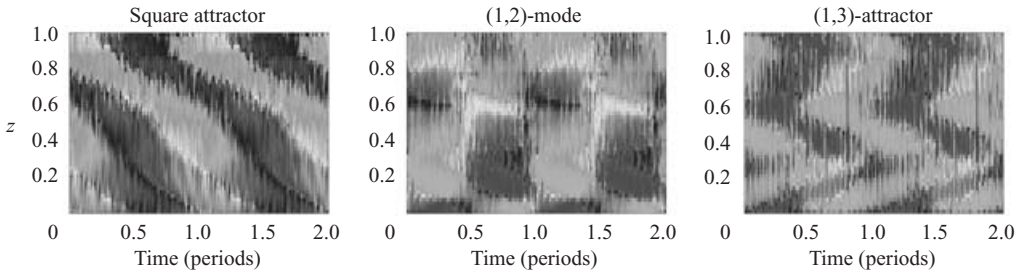

FIGURE 8. Angle $\phi = \arctan(w/u)$ as a function of depth and time on vertical lines for square attractor at $x = 0.99$, (1,2)-mode at $x = 0.84$ and (1,3)-attractor at $x = 0.32$. The pattern is shown twice (two identical periods, asynchronous sampling) to visualize the pattern of phase propagation better.

velocities in the measurements appears to agree well with the theoretical location of the attractor. It is difficult to give a clear interpretation of the phase pictures. The phase changes very rapidly across the line connecting the upper right corner to the lower left corner.

4.1.2. *Phase propagation*

As already mentioned, there is evidence that the (1,2)-mode behaves differently from the attractors. Phase changes take place at the same time over the whole cross-section. This is illustrated in figure 8. The parameter $\phi = \arctan(w/u)$ is plotted as function of time on a vertical line. Although this parameter is not equal to the phase, changes of ϕ are an indication of the phase changes. These sections are chosen such that for the square attractor the strongest branch of the attractor is included. The term *branch* refers to a part of the attractor between two boundary reflections. For the (1,2)-mode both cells are included and for the (1,3)-attractor the part where propagation is clearest. Asynchronous sampling was used to obtain a good time resolution. The pictures confirm that the flow field is nearly purely periodic. The single period is plotted twice to give a better impression of the continuity of phase propagation.

For the *square attractor*, phase shifts downwards with increasing time, implying phase propagation. This is in accordance with energy propagation downwards, as expected from the clockwise energy propagation along the attactor. There is a phase shift around $z = 1/2$, related to the transition of one branch of the attractor to another, but this is not visible in the black and white figure.

This is in strong contrast to the *(1,2)-mode*, which can be recognized as a standing wave. Patterns do not alter during half a period, then they change abruptly over the whole cross-section, to remain constant for the next half-period. The upper part of the upper cell and the lower part of the lower cell have the same phase, as do the lower part of the upper cell and the upper part of the lower cell. This is consistent with the idea of two counter-rotating cells (figure 2*h*).

For the *(1,3)-attractor* there is upward phase propagation in the lower part, downward propagation in the middle part and upward propagation in the upper part. This agrees well with the expected propagation directions and locations where this direction of phase propagation changes. Only in the uppermost part ($z > 0.7$) is there downward propagation again. This is not according to the predicted attractor shape, but can be attributed to a direct wave ray emanating from the upper left corner. Such a wave ray can be seen in the picture of U for this attractor in figure 7.

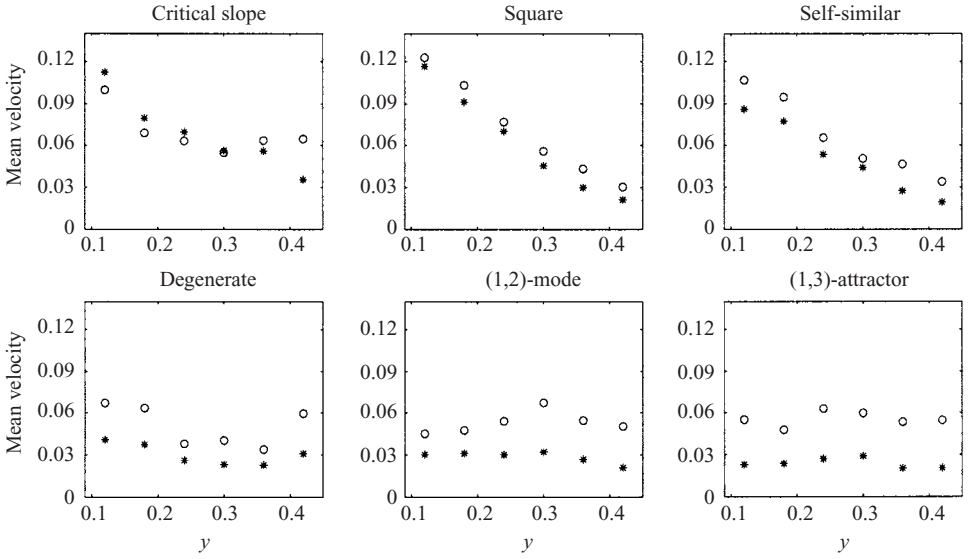

FIGURE 9. Mean speed the in x- ($\mathscr{U}$, circles) and z-directions ($\mathscr{W}$, stars) over the cross-section as a function of distance to the front wall for the different frequencies (table 1).

4.2. *Along-channel changes*

Measurements were taken at different y-positions. These can be used to study the structure of the attractor in the y-direction. To obtain an overall idea of the strength of the motion for different distances to the front wall, an average of the absolute value of the velocity components is computed per cross-section. The quantity $\mathscr{U}$ is defined as

$$\mathscr{U} = \frac{1}{NM} \sum_{n=1}^{N} \sum_{m=1}^{M} |u|_{nm}$$

with M the number of gridpoints and N the number of timesteps. $\mathscr{W}$ is similarly computed with w replacing u. This method does not distinguish wave motion from other types of motion, periodic or not. But the results appear to be instructive in comparing the y-dependent behaviour at the different frequencies, when interpreted in combination with other observations. The results, a very great compression of the data of almost all the observed vertical cross-sections, are presented in figure 9.

With increasing values of $\tan\theta$ (increasing frequency of the waves), u increases and w decreases. This implies that the difference between $\mathscr{U}$ and $\mathscr{W}$ increases. For a single frequency, this difference must be constant if the two-dimensional approach is valid, as is observed in the pictures of the square attractor and the (1,3)-attractor. Where this is not the case, for example for the critical slope attractor, other phenomena must contribute to the velocity field. In general the ratio $\mathscr{U}/\mathscr{W} \approx \tan\theta$ has the tendency to be a little too large; the u-component of the flow is somewhat too strong. For small y-values this might be an effect of the vorticity-conserving flow that is purely horizontal, but since the u-component of the vorticity-conserving flow should decrease rapidly with increasing y the ratio should also decrease, which is not observed. Another explanation is that slowly rotating steady vortices, that were observed over the flat part of the bottom in experiments with dye and that have nearly purely horizontal motion, account for this effect.

The most striking difference between the observations for the different frequencies is that for the critical slope attractor, the square and self-similar attractor there is a clear decay of $\mathscr{U}$ and $\mathscr{W}$ with increasing y whereas this is not the case for the other frequencies. This cannot be explained by the vorticity-conserving flow that contributes most near the front wall. There is no reason to expect that this contribution varies so strongly with the frequency.

Further and more detailed analysis of the structure of the wave field in the y-direction is obtained by comparing the ellipse parameters in successive cross-sections. For the critical slope and the self-similar attractor all the vertical cross-sections are presented. For the other frequencies only a description will be given.

The *critical slope attractor* is shown in figure 10 for all y-positions observed since its behaviour changes considerably in the y-direction. For $y > 0.3$ the phase could not be determined by matching with the horizontal cross-sections, since the horizontal cross-sections do not extend further. But it could be determined from the phase of the plane-averaged u-velocity, a method that does not work for the other frequencies but does reproduce the matching results for this specific frequency. The attractor is developed best at $y = 0.12$ where the motion is strongest. In the picture at $y = 0.18$ the left (diagonal) part of the attractor is clear but the part at the sloping wall is not; at $y = 0.24$ it is the other way round. At other locations either the left diagonal part or the part parallel to the sloping wall is clearly visible, but not in the same cross-section. Overall, the part near the sloping wall is most clearly visible. The general structure of the phase lines is the same over all y-values. The V-shape can be recognized even up to $y = 0.42$. But the absolute values vary considerably between the different sections. It appears that the phase decreases with increasing y-value, implying energy propagation from $y = 0$ towards the centre of the tank. Phase pictures that are about $1/5$ of the basin length (100 cm) apart have almost the same phase, indicating a wavelength of this size in the y-direction.

Instabilities and turbulence in the bottom boundary layer at the slope, as reported by Cacchione & Wunsch (1974) and Ivey & Nokes (1989) for critical internal waves, were not observed. Our observations do not resolve small-scale motion as well as theirs (schlieren pictures), but on the scale of our observations the motion along the sloping wall is described reasonably well by the two-dimensional attractor model.

In figure 11 the ellipse parameters are shown for the cross-sections of the *self-similar attractor*. All pictures have the same phase with respect to the sinusoidal forcing. Only for $y = 0.42$ is the phase uncertain; matching with horizontal cross-sections did not work since the motion is very weak there. The most striking feature of U is the rapid decrease with increasing y, with maximum values near the sloping wall where the waves were focused. This part of the attractor is still faintly visible at $y = 0.36$. Also, at $y = 0.12$ the shape of the attractor is slightly different: it is more narrow, the reflection at the sloping wall occurs somewhat higher, the reflection point at the bottom is shifted a little to the left and the reflection at the straight wall is at a lower position. There is strong horizontal motion near the top of the tank, which is also observed in Maas (2001). At $y = 0.18$ the attractor is most clearly visible. For $y > 0.3$, the motion for $x < 0.3$ is horizontal.

The phase lines are aligned well along the attractor. Outside the attractor, where the motion is weak, the phases are still rather coherent. Only for large y, where the attractor is hardly visible, do the structures become incoherent. The phases are more or less the same at the different y-positions; within the accuracy of the phase determination, no phase propagation can be observed.

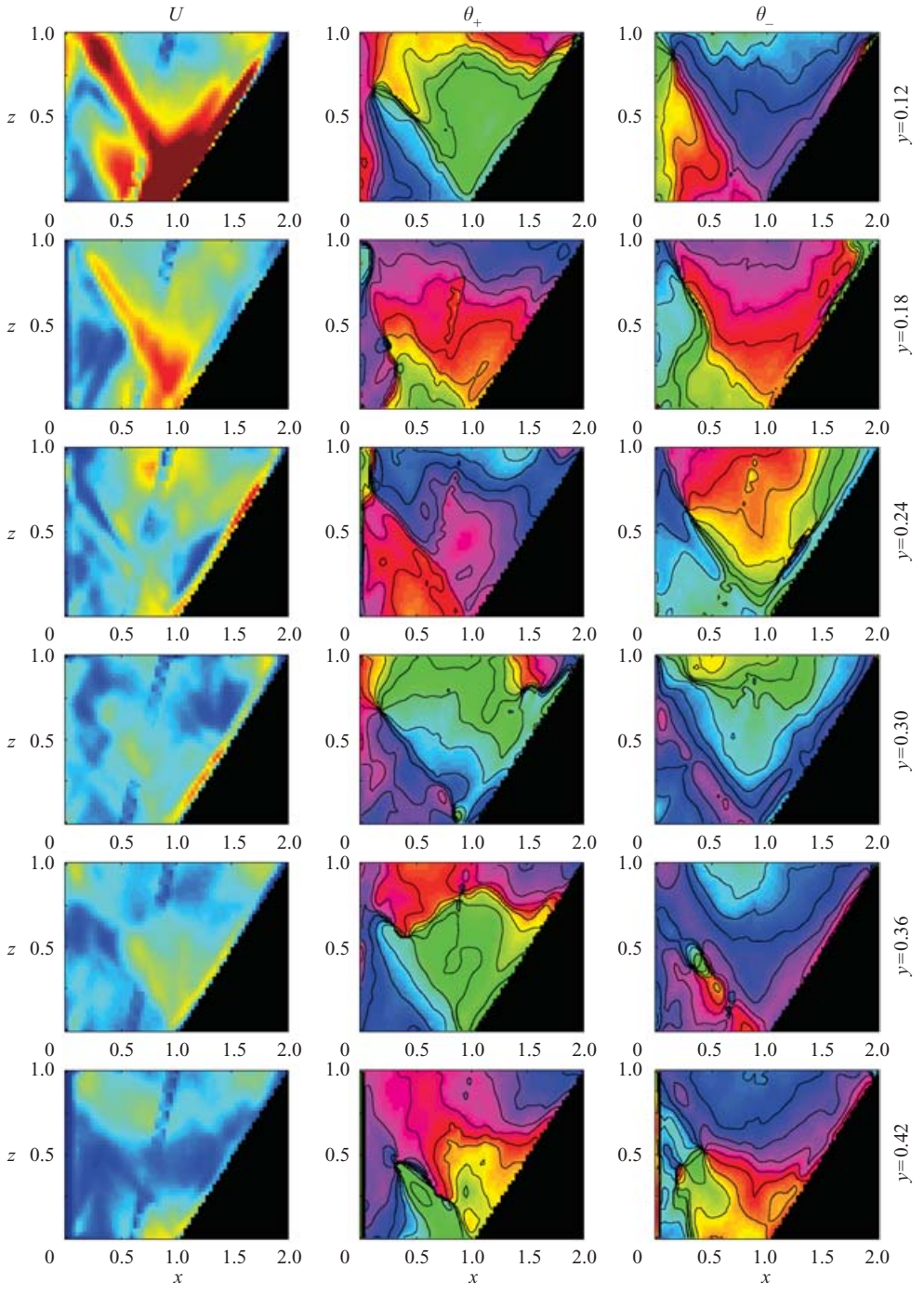

FIGURE 10. Ellipse parameters U, θ_+ and θ_- for the critical slope attractor at $y = 0.12$, $y = 0.18$, $y = 0.24$, $y = 0.3$, $y = 0.36$ and $y = 0.42$. The scale for U ranges from 0 (dark blue) to 0.4 cm s^{-1} (dark red).

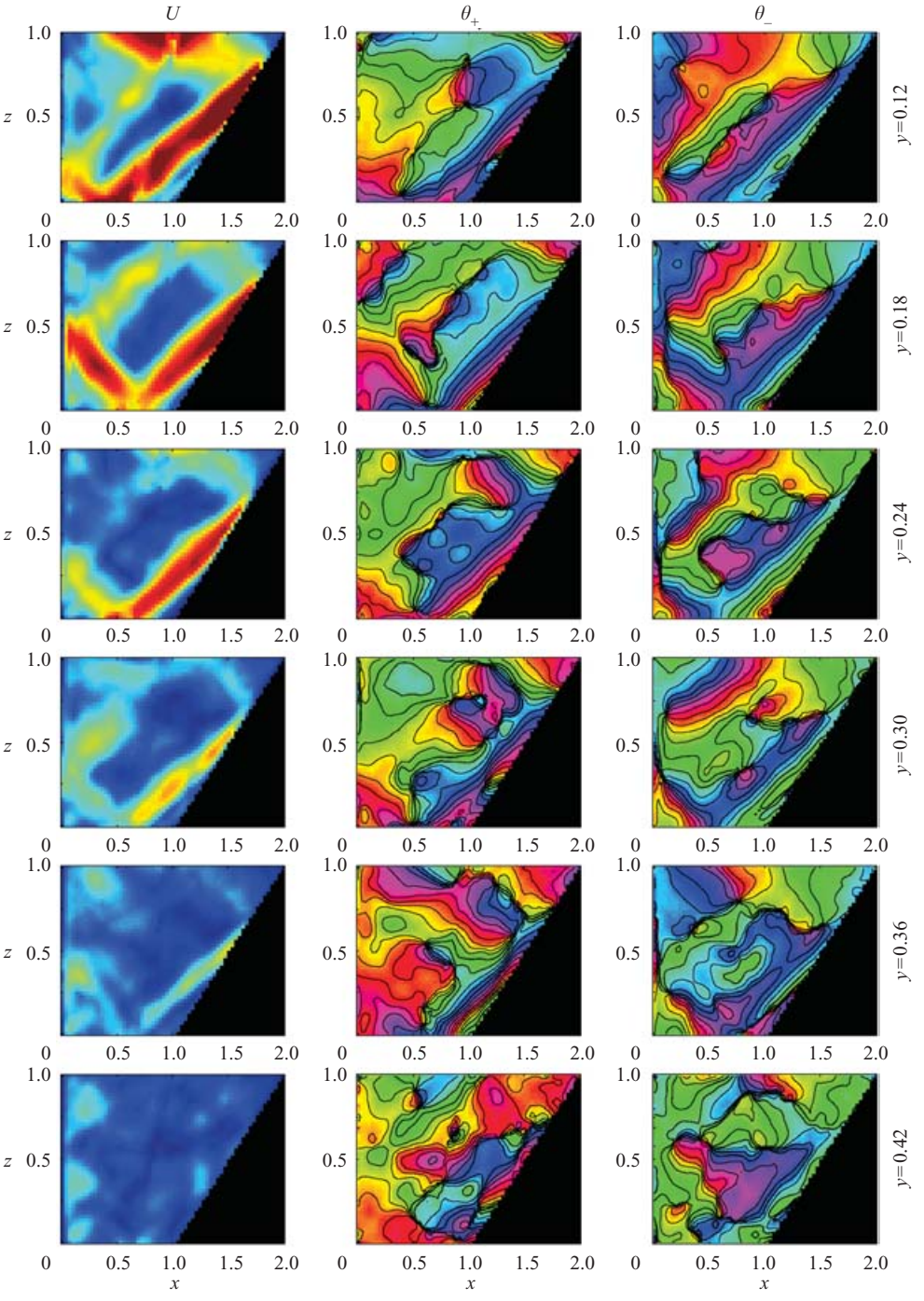

FIGURE 11. Ellipse parameters U, θ_+ and θ_- for the self-similar attractor at $y = 0.12$, $y = 0.18$, $y = 0.24$, $y = 0.3$, $y = 0.36$ and $y = 0.42$. The scale for U ranges from 0 to 0.4 cm s^{-1}.

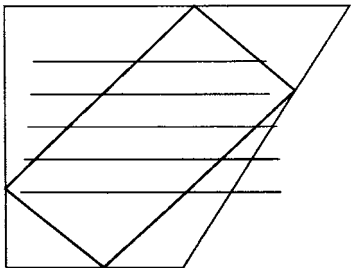

FIGURE 12. Location of horizontal cross-sections at $z = 0.29$, 0.41, 0.54, 0.66 and 0.79 with respect to a vertical cross-section.

For the *square attractor* (not shown) the behaviour is similar to that of the self-similar attractor; even the phases are the same in the equivalent part of the attractor.

We will briefly discuss the results for the other frequencies; they are not shown. The *degenerate attractor* is poorly developed at $y = 0.12$ where a lot of horizontal motion is present in the upper half of the cross-section. However, from the θ_--picture the line from the upper right to the lower left corner is clearly recognizable. The attractor is still visible at $y = 0.42$. U is somewhat larger at $y = 0.18$ and $y = 0.24$, but does not decay further with increasing y. There is no evidence for phase propagation in the y-direction, as far as could be observed.

The *(1,2)-mode* behaves somewhat similarly to the degenerate attractor. At $y = 0.12$ the cellular pattern is not visible from the U pictures although the θ_--pattern hints at a structure connecting the upper right to the lower right corner. The motion is again dominated by horizontal motion in the upper half. At $y = 0.24$ and $y = 0.3$ the cellular structure is most clear, but at $y = 0.36$ and $y = 0.42$ large parts can still be recognized from the U pictures. From the phase lines the structure is even clearer, especially the large upper cell with a sharp phase contrast diagonally through the cell. At $y = 0.12$ the phase with respect to the forcing could not be determined well; from the other cross-sections no significant phase propagation in the y-direction was observed.

The *(1,3)-attractor* is also not visible at $y = 0.12$; only in the middle of the cross-section are some areas of higher U visible. The phase structure has two more or less equal cells, one in the upper and one in the lower half of the section. At $y = 0.18$ parts of the attractor become visible, and at $y = 0.24$ the attractor is most clearly visible. At larger y-coordinates the structure is not as clear but large parts of the attractor are visible, and U hardly decreases. There were serious problems in matching with the horizontal cross-sections, so no conclusions can be drawn regarding the phase propagation in the y-direction.

4.3. *Horizontal cross-sections*

Measurements in horizontal cross-sections at different z-levels were taken for all frequencies. Unfortunately, only a small part of the tank could be observed for a single camera position, roughly from $x = 0.1$ to 1.6 and from $y = 0.1$ to 0.3. In figure 12 the positions of the horizontal cross-sections with respect to the self-similar attractor are illustrated. For the self-similar and square attractor, measurements were also taken that extend from $y = 0.3$ to 0.5, but they are of poor quality. There were more problems in obtaining satisfactory results. The metal frames around the glass plates inhibited the detection of particle motion at the edges of the glass

plates. By interpolation this was compensated to some extent. At some locations the measurements were poor due to the absence of tracer particles, which settled to the bottom very slowly during the experiment, or due to stains on the glass plates. In the horizontal, the vorticity-conserving flow dominates the fluid motion. To investigate the structure of the inertial wave field, this flow must be subtracted from the observed fields. Subtraction of the theoretically predicted field, while not exact, is also a source of errors. But it does eliminate the most obvious vorticity-conserving flow features.

As can be concluded from the previous paragraph, except for the critical slope attractor, the wave field does not change significantly in the y-direction, apart from intensity changes. The behaviour of each attractor is illustrated with results from a single (most illustrative) cross-section. The results are shown in figure 13 in terms of the ellipse parameters U and θ_-. Motion was dominantly clockwise; only where the intensity was very low was the motion anticlockwise, and therefore θ_+ is not shown. The black lines indicate the intersections with the theoretical attractor.

The cross-section of the *critical slope attractor* at $z = 0.29$ has most intense (although weak compared to the intensities observed in the vertical cross-sections) motion near the slope and around the theoretical line, but also closer to the straight wall. The change of intensity of parts of the attractor that was observed in the vertical cross-sections is not observed clearly in the horizontal cross-sections. In this area above the flat bottom some steady vortex activity was observed from dye experiments, but it is assumed to be filtered out by using the ellipse parameters. In the picture of θ_- one immediately sees the phase change in the y-direction, suggesting wave propagation in the negative y-direction, implying energy propagation from the front wall ($y = 0$) into the interior, with a wavelength that is a little larger than the cross-section, about 1/4. In the other horizontal cross-sections of this attractor there is no clear intense motion at the theoretically predicted locations. But again the phase propagation towards the front wall can be observed with a wavelength of about 1/4. This is consistent with the observations in the vertical cross-sections. Also, a phase change across the attractor in the x-direction is reproduced.

For the *square attractor* the cross-section at $z = 0.29$ is also shown. At this level the intersections with the strongest parts of the attractor are clearly visible from the high values of U. It is remarkable that these values do not persist over the length of the cross-section; the change around $x = 0.3$ for $y < 0.15$ is especially remarkable. The phase lines in this cross-section are not fully parallel to the y-axis but there is no clear phase propagation in this direction. Near $x = 0.2$ there is phase propagation in the positive x-direction (energy propagation towards $x = 0$), as already observed in the vertical cross-sections. The other cross-sections do not show consistent phase propagation directions in the y-direction either. Locations of intense motion cannot always be attributed to the attractor and are not continuous in the y-direction, although this was suggested by the results in the vertical cross-sections.

For the *self-similar attractor* the behaviour at $z = 0.54$ is illustrated. There is strong motion near the sloping wall, where the observations are slightly below the reflection point. The weak part of the attractor is either not or hardly visible. Phase lines are almost uniform in the y-direction. Near the branches of the attractor the directions of phase propagation are consistent with the observations in the vertical cross-sections: phase propagation towards the sloping wall near the sloping wall and towards the straight wall for the other branch. In the other cross-sections the energy is concentrated near the sloping wall and sometimes also around the other (in practice weak) branch of the attractor. Phase lines are dominantly uniform in the y-direction.

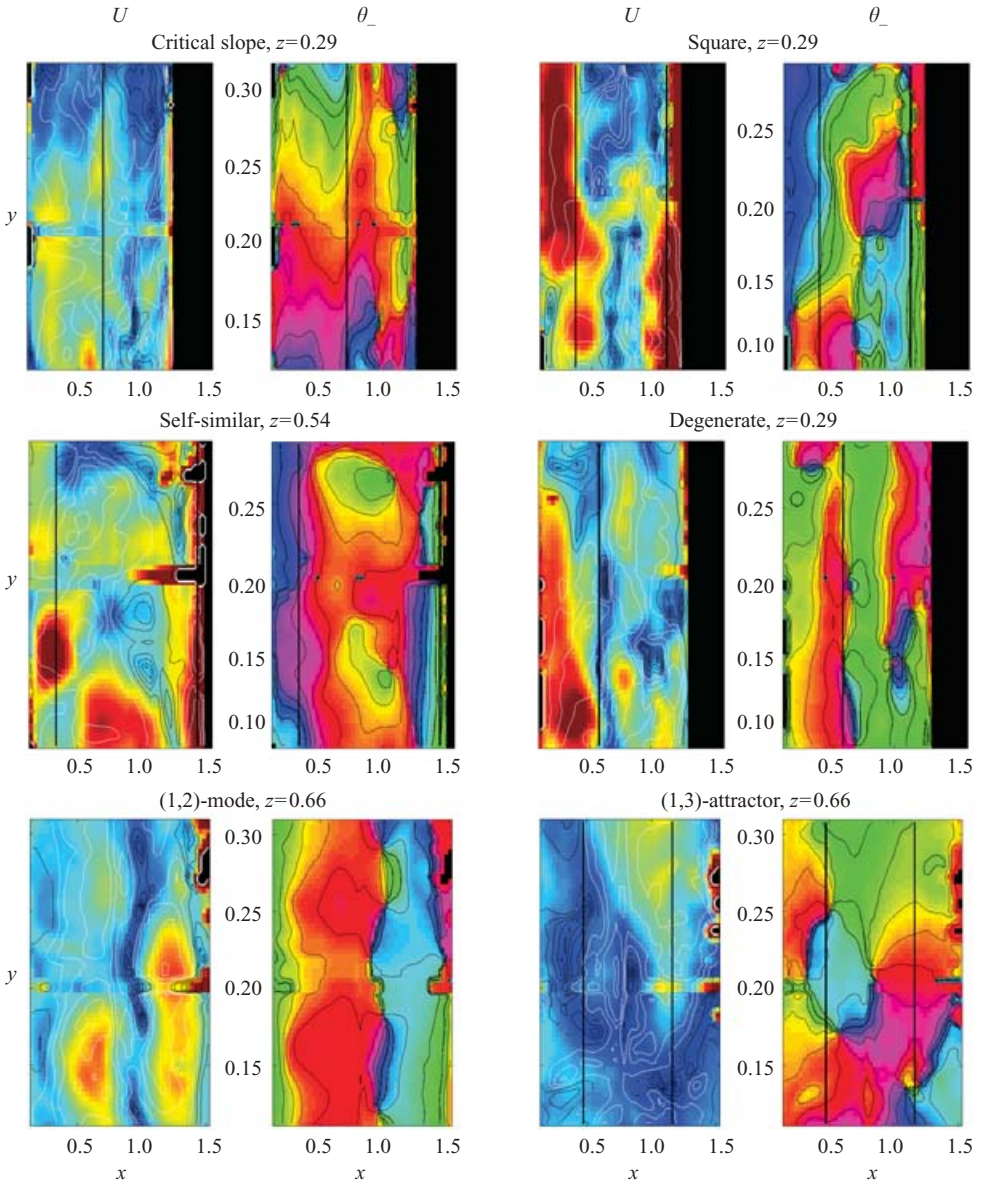

FIGURE 13. Horizontal cross-sections: ellipse parameters U and θ_{-}. The critical slope, square and degenerate attractor are shown at $z = 0.29$, the self-similar attractor is shown at $z = 0.54$ and the (1,3)-attractor and the resonant mode at $z = 0.66$. The black lines indicate the intersections with the theoretical two-dimensional attractor. The scale for U ranges from 0 (dark blue) to 0.4 cm s^{-1} (red), white contour lines indicate areas of clockwise motion, black lines of anticlockwise motion. The scale for θ_{-} is periodic. The black area to the right is the sloping wall. Slight perturbations around $y = 0.2$ are due to the frames around the glass plates.

The *degenerate attractor* has a remarkable line of weak motion around the theoretically predicted attractor, as already observed in the vertical cross-sections. There is strong motion near the straight wall. At other levels of observation there is also stronger motion on the sloping wall side of the attractor. Structures do not extend over the full y-range of the cross-sections. The attractor is identified by means

of the phase jump. Phase lines are roughly uniform in the y-direction. This behaviour is observed at all levels of observation.

The cross-section at $z = 0.66$ for the *(1,2)-mode* is through the centre of the upper cell ($x = 1$). At this centre there is no motion, which is confirmed by the observation. On both sides of this line of no motion there is rather strong motion. There is a phase jump over this line. The phase is clearly uniform in the y-direction. In all horizontal cross-sections the phase is dominantly uniform in the y-direction. In the x-direction there is a rapid phase change at the locations corresponding to the characteristic connecting the right upper corner to the right lower corner. The locations of intense motion are consistent with the vertical cross-sections, but again not continuous in the y-direction.

For the *(1,3)-attractor*, the cross-section at which most intense motion can be expected is the one at $z = 0.66$. Here the attractor is intersected close to the uppermost reflection at the sloping wall (focusing). For $y > 0.2$ there is indeed stronger motion. However, this motion is weaker than for the other attractors. At the other horizontal cross-sections there is nowhere really intense motion that can be related directly to the theoretically predicted attractor. Motion is everywhere less intense than for the other forcing frequencies. The phase patterns at different z-levels vary in both the x- and y-directions when comparing them. The main phase changes for the different cross-sections seem to be related to the characteristic connecting the upper right corner to the lower left corner of the tank. It is not possible to draw firm conclusions about propagation in the y-direction.

The imperfect correspondence between the observations in the horizontal and vertical planes is a point of concern. Still, the results have value. In particular, the critical slope attractor and the (1,2)-mode exhibit behaviour with a clear physical interpretation. For the other frequencies, the results show different structures for the different frequencies, but we are not yet able to interpret them. Therefore, we present some of the observations in the horizontal cross-sections and leave interpretation to the reader.

5. Discussion

The square attractor has already been observed in experiments by Maas (2001), in a smaller tank of similar shape. His result is reproduced and extended with observations of other attractor shapes and a standing wave, which are predicted for different frequencies. This shows that in three dimensions also waves can be focused towards an attractor. The two-dimensional theory correctly predicts the frequency interval over which a certain attractor exists and the shape of the attractor. Although viscosity will prevent the existence of a true line attractor, as a first-order description this theory is valuable.

A further aim was to study the three-dimensional behaviour of the waves. Separation of variables is not possible for a basin with a sloping boundary, and no alternative method of finding solutions is known to us. Therefore we have to rely fully on the observations.

The critical slope attractor is the only wave pattern with distinct three-dimensional behaviour on the scale of the observations. Its intensity decreases with increasing y and the location of the strongest motion on the attractor changes with y. There is clear phase propagation towards the front wall ($y = 0$) and energy propagation into the interior, with a wavelength in the y-direction between $1/5$ and $1/4$, as found from the observations in the vertical and horizontal cross-sections.

The other attractors do not exhibit clear phase propagation in the y-direction, only intensity changes are detected. The square and self-similar attractor are strong near $y = 0.12$ but their intensity decreases rapidly with increasing y. The degenerate and (1,3)-attractor and the standing mode are not as strong, but their strength is more or less constant for increasing y.

At least part of the variation of the strength of the motion with the y-position must be attributed to the forcing mechanism, which in the present experiment is weak modulation of the rotation rate. Another experiment was done in which waves were excited by a paddle in the corner of the tank (near $x = 0$, $z = 1$), extending over the full length of the tank. No modulation of the rotation was applied. This set-up had the disadvantage that a direct ray is visible, which is stronger than the wave attractor. It is difficult to provide enough energy to the fluid to generate an attractor without introducing nonlinear effects. The few measurements for this set-up, for an attractor in the (1,1)-domain, show more intense motion towards the centre of the tank ($y = 0.3$) than near the front wall ($y = 0.12$). So the distribution of energy in the y-direction seems not to be an intrinsic property of the wave field.

It is likely that when waves are generated by modulation, direct forcing near the endwalls, where the vorticity-conserving flow has a cross-slope component, dominates the indirect generation (Ekman pumping). It remains puzzling why this decrease with increasing distance to the endwalls is not observed for the weaker attractors.

The (1,2)-mode looks like an attractor in vertical cross-sections, since the most intense motion is confined to narrow bands. However, in time the velocity changes occur almost uniformly over the vertical cross-section, so the waves are not travelling waves. Contrary to the common idea that the standing modes are the strongest motions, the motion is weak, compared to the square and self-similar attractors. Therefore, and for the following reason, the term 'resonant mode' is not appropriate in this case. The standing wave does not suffer from nonlinear breakdown phenomena as studied by McEwan (1970) and Manasseh (1992) for resonant modes in a cylinder. Asynchronous sampling could be applied without any difficulty. This indicates a steady pattern for the full period of observation, which is more than half an hour and spans more than 70 rotation periods and several planes of observation. Apparently the rotation rate and excitation strength, which play an important role in the growth of the instabilities according to McEwan (1970), are low enough. We speculate that focusing of the waves during part of the oscillation period prevents instabilities from growing, since it forces unstructured motion back to structured motion, a process that will not take place in a rotating cylinder. Also, the damping rate may be increased due to the smaller scales imposed by wave focusing.

The wave rays connecting the corners of the tank for the (1,2)-mode are clearly visible as lines of low motion and sharp phase contrast. This is probably a result of the forcing function. Wood (1965) calculated the nature of such lines of discontinuity for a rotating and precessing cylinder. Their exact properties (discontinuity in velocity or velocity gradient) depend on the number of reflections it takes before the lines are reflected back onto themselves. Baines (1967) also made calculations regarding these lines, for a rotating cylinder (radius a) in which inertial waves were forced by oscillation of the end caps. At these end caps the vertical velocity is essentially prescribed as $f(r)\cos\omega t$ with r the radial coordinate. Lines of discontinuity of the velocity occur if $f'(r)$ has discontinuities and if $f'(a) \neq 0$ and in some cases if $f''(a) \neq 0$. Maas & Lam (1995) illustrate, for the bucket (two sloping walls), that the shape of the resonant mode is strongly dependent on the exact properties of a function on the boundary. This function prescribes the information carried

by the characteristics (partial pressure) and replaces the prescription of the forcing mechanism. Only if this function has a derivative equal to 0 at the boundaries of the region for which it can be prescribed, are the cells smooth and there are no lines of discontinuity. In an experiment, one cannot prescibe this function at will. It is determined by the chosen setting and in general the condition of zero derivative will not hold. For example McEwan (1970) reports lines of strong shear emanating from the corners of the rotating cylinder. Also Greenspan (1968*a*) and Beardsley (1970) report wave rays stemming from the upper corners of rotating cones, that are seen to reflect a few times at the boundaries. They applied modulation of the rotation frequency to generate waves via Ekman pumping as we did. However, in the rotating cones the vorticity-conserving flow will not have a cross-slope component, which is the primary forcing in our case. We also sometimes observed a wave ray emanating from the corner at $x = 0$, $z = 1$ for the square and self-similar attractors.

These are not many experiments in the literature in which focusing of inertial waves is studied experimentally. The emphasis has been on resonant modes and their interaction and the interaction with the background flow. At first sight, the article by Beardsley (1970) is not an exception, but his results for the truncated cone (frustum) can be interpreted in terms of wave attractors. Plotting the Lyapunov exponent for his configuration yields a structure similar to that of figure 1(*b*), with windows of attractors and isolated frequencies for which resonances occur. The amplitude maxima in the pressure sensors that he used do not occur for the simplest resonant modes, but for frequencies close to the strongest windows of attraction. Henderson & Aldridge (1992) solve the equations for the frustum numerically and interpret the results in terms of eigenmodes. However, their numerical grid is not fine enough to resolve a wave attractor. They also analytically compute two special ray paths, connecting the upper and the lower corners respectively, and compare the corresponding propagation angle (frequency) with the numerically determined eigenfrequency (their figure 4). The two paths yield two slightly different values for the propagation angle. For an eigenmode, this angle should be unique. These special ray paths can be identified with the upper and lower boundary of the window of an attractor, thus explaining the appearance of the two different values.

To conclude: the two-dimensional theory correctly predicts the frequencies and basic shapes of the attractors and the standing mode, but the three-dimensional structure has not been resolved satisfactorily. It would be interesting to have observations near $y = 0$ and for the other half of the tank to see if the behaviour is more or less symmetric or antisymmetric with respect to $y = 1/2$ or if there is a preferential direction. Possibly, rapid changes near the walls, as predicted for inertial waves in a rectangular box (Maas 2003) could not be resolved well in our experiments. Similar experiments have been carried out in a smaller tank. They can shed more light on the three-dimensional behaviour of the waves and we hope to report on them in the future (Manders & Maas 2003). Also numerical simulations would be instructive.

The authors gratefully acknowledge the help during the experiments from the team of the Coriolis Laboratory (Grenoble) and Frans Eijgenraam, Ronald de Leeuw and Theo Gerkema (NIOZ). We would also like to thank Maartje Rienstra for her contribution to the experiments, data processing and discussion. We thank M. Rieutord, J. Sommeria and an anonymous referee for constructive remarks. This project was financially supported by the European Community (program 'Access to major research infrastructures') and A. M. is supported by the Dutch organization for Scientific Research NWO (project number 620-61-392).

Appendix. Vorticity-conserving flow

Here the structure of the vorticity-conserving flow is derived for a tank with a sloping wall. This tank has length L and height H_0 over the flat bottom; the water depth $H(x)$ is function of x only. The top of the basin has width $2B$ and the bottom has width B. The angular frequency $\Omega(t)$ consists of a weak modulation $\epsilon\Omega_1(t)$, $\epsilon \ll 1$, around the steady-state value Ω_0.

When studying spin-up problems in tanks with a sloping bottom, van Heijst *et al.* (1994) found that the exact solution for a wedge-shaped tank ($2B = H_0$, $L \gg H_0$) showed almost no variation in the vertical direction. This justified the shallow-water approximation for a tank with a sloping bottom that is long in the along-slope direction ($L \gg H_0$). Since our tank has a closely related geometry, we follow their approach and also make this approximation. This enables the calculation of an exact solution for the approximated problem.

The first step is to compute the vorticity $\nabla \times \partial \boldsymbol{u}/\partial t$ for the linearized momentum equations (2.1). Because of the shallow-water conditions, variations of u and v with z are neglected. The vertical vorticity equation is

$$\frac{\partial}{\partial t}\left(\frac{\partial v}{\partial x} - \frac{\partial u}{\partial y}\right) = -2\Omega_0\left(\frac{\partial u}{\partial x} + \frac{\partial v}{\partial y}\right) - 2\frac{\partial \Omega_1}{\partial t}. \tag{A 1}$$

Integrating the continuity equation (2.2) over the vertical, with boundary conditions of no flow through the bottom and the top, results in the equation for the conservation of mass:

$$\frac{\partial}{\partial x}(uH) + \frac{\partial}{\partial y}(vH) = 0. \tag{A 2}$$

Substitution in (A 1), division by H and introduction of $\zeta = \partial v/\partial x - \partial u/\partial y$ for the vertical vorticity, gives

$$\frac{1}{H}\frac{\partial \zeta}{\partial t} = \frac{2\Omega_0}{H^2}\left(u\frac{\partial H}{\partial x} + v\frac{\partial H}{\partial y}\right) - \frac{2}{H}\frac{\partial \Omega_1}{\partial t}. \tag{A 3}$$

Rearranging terms shows that (A 3) is the lowest order of the total time derivative (material derivative)

$$\frac{\mathrm{D}}{\mathrm{D}t}\left(\frac{\zeta + 2\Omega}{H}\right) = 0 \tag{A 4}$$

which means that individual particles conserve potential vorticity:

$$\frac{\zeta + 2\Omega}{H} = C.$$

Before the modulation starts, the fluid is in solid-body rotation with angular frequency Ω_0. This gives the constant C the value $2\Omega_0/H$. Take the modulation of the form

$$\Omega = \Omega_0(1 + \epsilon \sin \omega t)$$

so that the perturbation vertical vorticity is

$$\zeta = \frac{\partial v}{\partial x} - \frac{\partial u}{\partial y} = -2\Omega_0 \sin \omega t. \tag{A 5}$$

Introduce the mass transport stream function

$$\Xi(x, y, t) = \Psi(x, y) \sin \omega t \tag{A 6}$$

with the spatial part defined as

$$Hu = -\frac{\partial \Psi}{\partial y}, \qquad Hv = \frac{\partial \Psi}{\partial x}. \tag{A 7}$$

Substitution of these expressions into (A 5) leads to

$$\nabla^2 \Psi - \frac{1}{H}(\nabla H \cdot \nabla \Psi) = -2\Omega_0 H. \tag{A 8}$$

The boundary conditions are

$$\Psi = 0 \text{ at } x = 0,\ x = 2B \text{ and at } y = 0,\ y = L. \tag{A 9}$$

The bottom profile H of our tank is given by

$$H(x) = \begin{cases} H_0, & 0 \leqslant x < B \\ H_0(1 - (x - B)/B), & B \leqslant x \leqslant 2B. \end{cases} \tag{A 10}$$

Substitution of this bottom profile naturally splits the equation for the stream function in two parts: one for the flat bottom and one for the sloping bottom, denoted by Ψ_1 and Ψ_2 respectively:

$$\left.\begin{array}{lll} \Psi_1: & \nabla^2 \Psi_1 = -2\Omega_0 H_0, & 0 \leqslant x < B \\ \Psi_2: & \nabla^2 \Psi_2 + \dfrac{1}{H_0(2 - x/B)} \dfrac{H_0}{B} \dfrac{\partial \Psi_2}{\partial x} = -2\Omega_0 H_0 \left(1 - \dfrac{x - B}{B}\right), & B \leqslant x \leqslant 2B. \end{array}\right\} \tag{A 11}$$

These equations can be solved separately but the solutions are subject to matching conditions at $x = B$, requiring continuity and smoothness.

For convenience the equations will be scaled:

$$x = B(x' + 1),\ y = L(y' + 1/2),\ \Psi = -2B^2 H_0 \Omega_0 \Psi'. \tag{A 12}$$

The dimensionless equations (primes dropped from now on) are

$$\Psi_{1xx} + \mu^2 \Psi_{1yy} = 1, \tag{A 13}$$

$$\Psi_{2xx} + \frac{1}{1 - x}\Psi_{2x} + \mu^2 \Psi_{2yy} = 1 - x, \tag{A 14}$$

where $\mu = B/L$, with boundary conditions

$$\begin{array}{llll} \Psi_1 = 0 & \text{at} \quad x = -1 & \text{and at} & y = \pm 1/2, \\ \Psi_2 = 0 & \text{at} \quad x = 1 & \text{and at} & y = \pm 1/2, \\ \Psi_1 = \Psi_2 & \text{at} \quad x = 0, & & \\ \dfrac{\partial \Psi_1}{\partial x} = \dfrac{\partial \Psi_2}{\partial x} & \text{at} \quad x = 0. & & \end{array} \tag{A 15}$$

A solution of the homogeneous part of (A 13) is obtained by separation of variables, leading to

$$\Psi_{1h} = P \cosh\left(\frac{\lambda}{\mu} y\right) \sin(\lambda(1 + x)). \tag{A 16}$$

A particular solution to (A 13) is $\Psi_{1p} = \frac{1}{2}(x + 1)^2 + c_1(x + 1)$. The complete solution satisfies the boundary condition at $x = -1$. The constants P and c_1, and the eigenvalue λ are to be determined from matching of the solutions at $x = 0$ and the boundary conditions at $y = \pm 1/2$.

Separation of variables for the homogeneous part of (A 14) leads to a solution in terms of the first-order Bessel function J_1:

$$\Psi_{2h} = R\cosh\left(\frac{\lambda}{\mu}y\right)(1-x)J_1(\lambda(1-x)). \tag{A 17}$$

A particular solution to (A 14) is $\Psi_{2p} = \frac{1}{3}(1-x)^3 + c_2(1-x)^2$. The complete solution satisfies the boundary condition at $x=1$; the constants R, c_2 and the eigenvalue λ are to be determined from matching at $x=0$ and the boundary conditions at $y=\pm 1/2$.

Matching at $x=0$ gives the values $c_1=-7/9$ and $c_2=-11/18$ and leads to the eigenvalue equation

$$J_0(\lambda)\sin\lambda + J_1(\lambda)\cos\lambda = 0 \tag{A 18}$$

which results in a discrete spectum of eigenvalues λ_n that can be approximated numerically and a series of P_n and R_n.

Now that the general structure of the solution is complete, the constants P_n and R_n can be computed from the condition $\Psi_h + \Psi_p = 0$ at $y = \pm\frac{1}{2}$ for both domains, using an orthogonal set of eigenfunctions. The eigenfunctions are

$$e_m = \begin{cases} \dfrac{\sin\lambda_m(1+x)}{\sin\lambda_m}, & -1 \leqslant x < 0 \\ \dfrac{J_1(\lambda_m(1-x))}{J_1(\lambda_m)}, & 0 \leqslant x \leqslant 1. \end{cases} \tag{A 19}$$

They are orthogonal with respect to the weight function w,

$$w = \begin{cases} 1, & -1 \leqslant x < 0 \\ 1-x, & 0 \leqslant x \leqslant 1 \end{cases}$$

and the orthogonality relation is

$$\int_{-1}^{0} \frac{\sin(\lambda_m(1+x))\sin(\lambda_n(1+x))}{\sin\lambda_m \sin\lambda_n}\,\mathrm{d}x + \int_0^1 (1-x)\frac{J_1(\lambda_m(1-x))J_1(\lambda_n(1-x))}{J_1(\lambda_m)J_1(\lambda_n)}\,\mathrm{d}x = \delta_{nm}\frac{1}{2}\left(\frac{1}{\lambda_n}\frac{\cos\lambda_n}{\sin\lambda_n} + \frac{2}{\sin^2\lambda_n}\right). \tag{A 20}$$

The matching condition at $x=0$ relates the constants P and R as $P_n\sin(\lambda_n) = R_n J_1(\lambda_n) = Q_n$ where Q_n is introduced for convenience. Q_n is determined by the boundary condition at $y=\pm 1/2$. It is computed by inserting $y=1/2$ in the full solution, multiplying by the eigenfunctions and integration over the domain

$$\int_{-1}^{0} \Psi_{1h}\left(x, \tfrac{1}{2}\right)e_m\,\mathrm{d}x + \int_0^1 \Psi_{2h}\left(x, \tfrac{1}{2}\right)e_m\,\mathrm{d}x + \int_{-1}^{0}\Psi_{1p}(x)e_m\,\mathrm{d}x + \int_0^1 \Psi_{2p}(x)e_m\,\mathrm{d}x = 0. \tag{A 21}$$

leading to

$$\begin{aligned} Q_n = \frac{2}{\cosh\dfrac{\lambda_n}{2\mu}\left(\dfrac{1}{\lambda_n}\dfrac{\cos\lambda_n}{\sin\lambda_n} + \dfrac{2}{\sin^2\lambda_n}\right)} \Bigg\{ & \frac{1}{J_1(\lambda_n)}\left(-\frac{1}{\lambda_n^3}J_1(\lambda_n)S_{2,0}(\lambda_n)\right. \\ & \left. - \frac{1}{2\lambda_n^2}J_0(\lambda_n)S_{3,1}(\lambda_n) + \frac{11}{18}\frac{1}{\lambda_n}J_2(\lambda_n)\right) \\ & - \left(\frac{5}{18\lambda_n} + \frac{1}{\lambda_n^3}\right)\frac{\cos\lambda_n}{\sin\lambda_n} - \frac{2}{9\lambda_n^2} + \frac{1}{\lambda_n^3\sin\lambda_n}\Bigg\}. \end{aligned} \tag{A 22}$$

The functions $S_{2,0}$ and $S_{3,1}$ are Lommel's functions (Magnus, Oberhettinger & Soni 1966).

The complete solution in the original coordinates is given by

$$\Psi = -2B^2 H_0 \Omega_0 \times \begin{cases} \displaystyle\sum_{n=1}^{\infty} \frac{Q_n}{\sin\lambda_n} \cosh\left(\frac{\lambda_n L}{B}\left(\frac{y}{L}-\frac{1}{2}\right)\right) \sin\left(\lambda_n \frac{x}{B}\right) + \frac{1}{2}\left(\frac{x}{B}\right)^2 - \frac{7}{9}\left(\frac{x}{B}\right), & 0 \leqslant x < B \\ \displaystyle\sum_{n=1}^{\infty} \frac{Q_n}{J_1(\lambda_n)} \cosh\left(\frac{\lambda_n L}{B}\left(\frac{y}{L}-\frac{1}{2}\right)\right) \left(1-\frac{x-B}{B}\right) J_1\left(\lambda_n\left(1-\frac{x-B}{B}\right)\right) \\ \quad + \frac{1}{3}\left(1-\frac{x-B}{B}\right)^3 - \frac{11}{18}\left(1-\frac{x-B}{B}\right)^2, & B \leqslant x \leqslant 2B. \end{cases} \tag{A 23}$$

The velocities can be derived via

$$u = -\frac{1}{H(x)}\frac{\partial\Psi}{\partial y}, \quad v = \frac{1}{H(x)}\frac{\partial\Psi}{\partial x} \tag{A 24a,b}$$

This results in an 'ellipsoidal' flow, with maximum velocities at the middle of the boundaries and with zero velocity above the flat part, at $x \approx 0.39 \times 2B$.

REFERENCES

Aldridge, K. D. & Toomre, A. 1969 Axisymmetric inertial oscillations of a fluid in a rotating spherical container. *J. Fluid Mech.* **37**, 307–323.

Baines, P. G. 1967 Forced oscillations of an enclosed rotating fluid. *J. Fluid Mech.* **30**, 533–546.

Beardsley, R. C. 1970 An experimental study of inertial waves in a closed cone. *Stud. Appl. Maths* **49**, 187–196.

Bretherton, P. 1964 Low frequency oscillations trapped near the equator. *Tellus* **XVI** (2), 181–185.

Bryan, G. 1889 The waves on a rotating liquid spheroid of finite ellipticity. *Phil. Trans. R. Soc. Lond.* **180**, 187–219.

Cacchione, D. & Wunsch, C. 1974 Experimental study of internal waves over a slope. *J. Fluid Mech.* **66**, 223–239.

Cartan, M. E. 1922 Sur les petites oscillations d'une masse de fluide. *Bull. Sciènces Math.* **46**, 317–369.

Fincham, A. & Spedding, G. R. 1997 Low cost, high resolution dpiv for measurement of turbulent fluid flow. *Exps. Fluids* **23**, 449–462.

Görtler, H. 1943 Über eine Schwingungserscheinung in Flüssigkeiten mit stabiler Dichteschichtung. *Z. Angew. Math. Mech.* **23**, 65–71.

Görtler, H. 1944 Einige Bemerkungen über Strömungen in rotierenden Flüssigkeiten. *Z. Angew. Math. Mech.* **25**, 210–214.

Greenspan, H. P. 1968*a* On the inviscid theory of rotating fluids. *Stud. Appl. Maths* **48**, 19–28.

Greenspan, H. P. 1968*b* *The Theory of Rotating Fluids*. Cambridge University Press.

van Heijst, G. J. F., Maas, L. R. M. & Williams, C. W. M. 1994 The spin-up of fluid in a rectangular container with a sloping bottom. *J. Fluid Mech.* **265**, 125–159.

Henderson, G. A. & Aldridge, K. D. 1992 A finite-element method for inertial waves in a frustum. *J. Fluid Mech.* **234**, 317–327.

Israeli, M. 1972 On trapped oscillations of rotating fluids in spherical shells. *Stud. Appl. Maths* **51**, 219–237.

Ivey, G. N. & Nokes, R. I. 1989 Vertical mixing due to the breaking of critical internal waves on sloping boundaries. *J. Fluid Mech.* **204**, 479–500.

Kelvin, Lord 1880 Vibrations of a columnar vortex. *Phil. Mag.* **10**, 155–168.

LeBlond, P. H. & Mysak, L. A. 1978 *Waves in the Ocean*. Elsevier.

Maas, L. R. M. 2001 Wave focusing and ensuing mean flow due to symmetry breaking in rotating fluids. *J. Fluid Mech.* **437**, 13–28.

Maas, L. R. M. 2003 On the amphidromic structure of inertial waves in a rectangular parallelepiped. *Fluid Dyn. Res.* (in press).

Maas, L. R. M., Benielli, D., Sommeria, J. & Lam, F.-P. A. 1997 Observation of an internal wave attractor in a confined, stably stratified fluid. *Nature* **388**, 557–561.

Maas, L. R. M. & van Haren, J. J. M. 1987 Observations on the vertical structure of tidal and inertial currents in the central North Sea. *J. Mar. Res.* **45**, 293–318.

Maas, L. R. M. & Lam, F.-P. A. 1995 Geometric focusing of internal waves. *J. Fluid Mech.* **300**, 1–41.

Magnus, W., Oberhettinger, F. & Soni, R. P. 1966 *Formulas and Theorems for the Special Functions of Mathematical Physics,* 3rd edn. Springer.

Manasseh, R. 1992 Breakdown regimes of inertia waves in a precessing cylinder. *J. Fluid Mech.* **243**, 261–296.

Manders, A. M. M. & Maas, L. R. M. 2003 On the three-dimensional structure of the inertial wave field in a rectangular basin with one sloping boundary. *Fluid Dyn. Res.* (submitted).

McEwan, A. D. 1970 Inertial oscillations in a rotating fluid cylinder. *J. Fluid Mech.* **40**, 603–640.

Oser, H. 1958 Experimentelle Untersuchung über harmonische Schwingungen in rotierenden Flüssigkeiten. *Z. Angew. Math. Mech.* **38** (9/10), 386–391.

Phillips, O. M. 1963 Energy transfer in rotating fluids by reflection of inertial waves. *Phys. Fluids* **6**, 513–520.

Rieutord, M., Georgeot, B. & Valdettaro, L. 2001 Inertial waves in a rotating spherical shell: attractors and asymptotic spectrum. *J. Fluid Mech.* **435**, 103–144.

Stern, M. E. 1963 Trapping of low frequency oscillations in an equatorial 'bounday layer'. *Tellus* **XV** (3), 246–250.

Stewartson, K. 1971 On trapped oscillations of a rotating fluid in a thin spherical shell. *Tellus* **XXII** (6), 506–510.

Stewartson, K. 1972 On trapped oscillations of a rotating fluid in a thin spherical shell ii. *Tellus* **XXIV** (4), 283–286.

Stewartson, K. & Rickard, J. A. 1969 Pathological oscillations of a rotating fluid. *J. Fluid Mech.* **5**, 577–592.

Tolstoy, I. 1973 Wave Propagation. *McGraw-Hill.*

Veronis, G. 1970 The analogy between rotating and stratified fluids. *Annu. Rev. Fluid Mech.* **2**, 37–66.

Wood, W. W. 1965 Properties of inviscid, recirculating flows. *J. Fluid Mech.* **22**, 337–346.

Wunsch, C. 1969 Progressive internal waves on slopes. *J. Fluid Mech.* **35**, 131–144.